IEEE Access
Multidisciplinary | Rapid Review | Open Access Journal

Received May 3, 2019, accepted May 31, 2019, date of publication June 13, 2019, date of current version June 27, 2019.

Digital Object Identifier 10.1109/ACCESS.2019.2922320

Investigation of the End Leakage Flux in Fractional Slot Concentrated-Winding Surface Permanent Magnet Machines

XIANBAO CHEN[1], HONGYU SHU[1,2], YITONG SONG[1], SHUANG LUO[1], AND CHENG GUO[1]
[1]School of Automotive Engineering, Chongqing University, Chongqing, 400044 China
[2]State Key Laboratory of Mechanical Transmission, Chongqing University, Chongqing, 400044 China

Corresponding author: Hongyu Shu (shyxianbao@163.com)

This work was supported by the Chongqing Provincial Natural Science Foundation of China under Grant cstc2018jcyjAX0077.

ABSTRACT When the end leakage flux or end leakage inductance cannot be ignored in a permanent magnet (PM) machine (e.g., a PM machine with a short axial length), the analysis of the machine is a time-consuming three-dimensional (3-D) issue. Existing research has made the end leakage inductance no longer to hinder that the performance calculation of fractional slot concentrated-winding surface permanent magnet (FSCWSPM) machines is simplified into a time-saving 2-D issue. However, no such mature research exists for end leakage flux. This paper proposes a novel end leakage flux function that can be used to accurately quantify the end leakage flux of FSCWSPM machines. Then, based on sensitivity research and regression analysis, a parametric model is established to quickly construct the end leakage flux function. Thus, even for FSCWSPM machines with nonnegligible end leakage flux, the results comparable to those from the 3-D finite element method (FEM) can be easily obtained using the proposed end leakage flux function and parametric model to revise the results from 2-D FEM. Moreover, the application of the above function and model is briefly described. Finally, FEM and experimental results are used to verify the calculation precision, adaptability, and timeliness of the proposed methodology.

INDEX TERMS End leakage flux, end leakage flux function, fractional slot concentrated-winding surface permanent magnet (FSCWSPM) machine, parametric model.

I. INTRODUCTION

Permanent magnet (PM) machines have been widely applied due to their advantages [1]. Additionally, because fractional slot concentrated-winding surface permanent magnet (FSCWSPM) machines have short end windings and small cogging torques, they have been extensively investigated [2]–[5]. However, when the end leakage flux of PMs [6] or the end leakage inductance caused by end windings [7] cannot be neglected in a PM machine (e.g., a PM machine with a short axial length) [8]–[11], the analysis of the machine is a time-consuming three-dimensional (3-D) issue. The 3-D solution is difficult to apply during initial design and optimization because the performance of the machine needs to be calculated dozens or even hundreds of times with continually modified dimension parameters.

The associate editor coordinating the review of this manuscript and approving it for publication was Wen-Sheng Zhao.

A parametric expression used to quickly and accurately calculate the end leakage inductance is established in [12]. The calculated end leakage inductance can be directly keyed in the design toolkit of Maxwell2D. Thus, the end leakage inductance no longer hinders that the analysis of PM machines is simplified into a time-saving 2-D issue.

In recent years, scholars have suggested using the end leakage flux function to quantify the end leakage flux of PM machines and then using the function to revise the 2-D analysis results to avoid the use of 3-D methods. The existing end leakage flux function can be classified by the end leakage flux coefficient (k_{end}) [13]–[17] and the air-gap flux density distribution function along the axial direction [18]–[22]. k_{end} is defined as the ratio of the phase fundamental back electromotive force (EMF) predicted by the 3-D finite element method (FEM) to that predicted by the 2-D FEM [13]. However, this approach attributes the influence of the end leakage inductance on the back EMF to the end leakage flux.

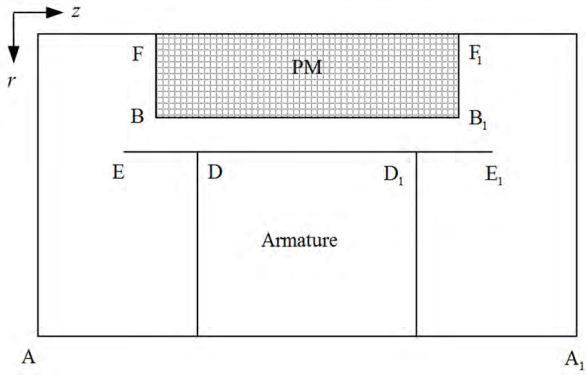

FIGURE 1. Full model in the axial direction used to solve the end leakage flux, where *r* and *z* are the radial and axial coordinates, respectively.

k_{end} is expressed as the ratio of the areas surrounded by the distribution curves of the peak radial air-gap flux density along the axial direction obtained from the 3-D and 2-D FEMs within the length of the armature [14]–[16]. Nevertheless, the results deduced from this method are susceptible to numerical errors, and the degree of interference is difficult to analyze, which will be illustrated in detail in the next section. A field domain for solving the end leakage flux of a PM machine is set up in [17], as shown in Fig. 1. The distribution of the magnetic vector potential in the field domain is calculated via 2-D FEM, and k_{end} is defined as the ratio of the difference of the magnetic vector potential between points F and F1 to that between points E and E1. However, the relative position between the rotor and the stator has a significant impact on the calculation results. The air-gap flux density distribution functions along the radial direction calculated from an analytic method (AM), an equivalent magnetic circuit (EMC) method, and the FEM were employed to correct the air-gap magnetic field predicted by 2-D methods in axial flux PM machines [18]–[22]. Notably, the radial direction in axial flux machines corresponds to the axial direction in the radial flux machines studied in this paper.

In addition to the above deficiencies, there is no parametric model that can rapidly construct the existing end leakage flux functions, which means that these functions cannot be obtained easily when the size of a PM machine is modified. In other words, the existing studies on end leakage flux may not sufficiently reduce the analysis of FSCWSPM machines with nonnegligible end leakage flux into a time-saving 2-D issue, which negatively impacts the initial design and optimization of these machines, as their performance needs to be analyzed many times with continually modified size parameters.

This paper aims to develop a methodology that can reduce the analysis of FSCWSPM machines to a 2-D issue, even if the end leakage flux cannot be ignored. In Section II, a novel end leakage flux function is proposed. In Section III, sensitivity research of the end leakage flux is implemented for FSCWSPM machines. In Section IV, a parametric model is established to rapidly construct the proposed end leakage flux function. In Section V, the application of the above function and model is simply described by taking the cogging torque calculation as an example. Finally, in Section VI, the accuracy, adaptability, and timeliness of the developed methodology are verified by analyzing four FSCWSPM machines with different sizes and output powers.

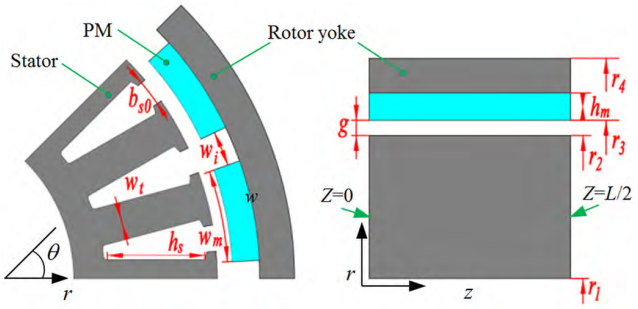

FIGURE 2. Topology with the hidden-windings of an FSCWSPM machine.

II. PROPOSED END LEAKAGE FLUX FUNCTION

Fig. 2 shows the hidden-windings topology of an FSCWSPM machine with 24 slots and 16 poles. Only half the machine in the axial direction is modeled because the machine is axially symmetric. Planes $z = 0$ and $z = L/2$ are the end face and the axial middle face of the machine, respectively, where z is the axial coordinate and L is the axial length. Table 1 lists four sets of parameters used for the topology. For the topology, open-circuit air-gap magnetic fields are calculated by the 2-D and 3-D FEMs. Fig. 3 depicts the radial and circumferential air-gap flux densities, namely, B_r and B_θ, calculated by the 3-D FEM when the first set of parameters is adopted. It can be seen that the flux densities decay rapidly at the end of the machine because of the end leakage flux.

TABLE 1. Specifications of the machine with four sets of dimension parameters.

Parameter (unit)	Values 1	Values 2	Values 3	Values 4
Axial length L (mm)	26	26	26	26
Stator inner diameter r_1 (mm)	43	43	43	43
Stator outer diameter r_2 (mm)	80	80	80	80
Slot depth h_{s2} (mm)	10.5	10.5	10.5	10.5
Tooth width w_t (mm)	4.8	4.8	4.8	4.8
Slot opening width b_{s0} (mm)	2.8	3.5	4.2	1.4
Air-gap length g (mm)	0.4	0.6	0.8	1
Rotor inner diameter r_3 (mm)	80.8	81.2	81.6	82
Rotor outer diameter r_4 (mm)	96.1	95	99.9	101.8
Magnet thickness h_m (mm)	2.75	2	4.25	5
Embrace α	0.8	0.8	0.8	0.8

Theoretically, the air-gap magnetic fields obtained by the 2-D and 3-D FEMs are the same in the axial middle of the machine where there is no end leakage flux; however, this is

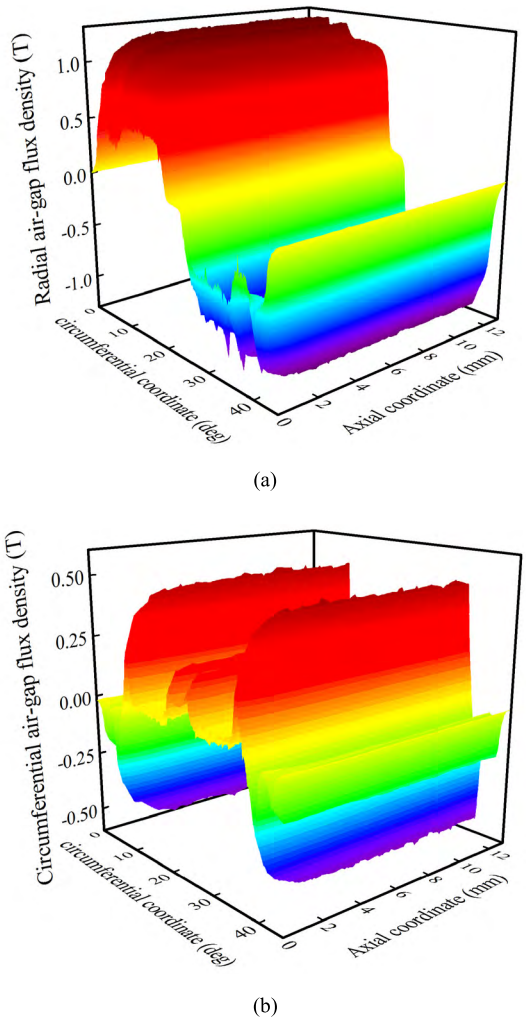

FIGURE 3. Air-gap flux densities simulated by the 3-D FEM. (a) Radial component. (b) Circumferential component.

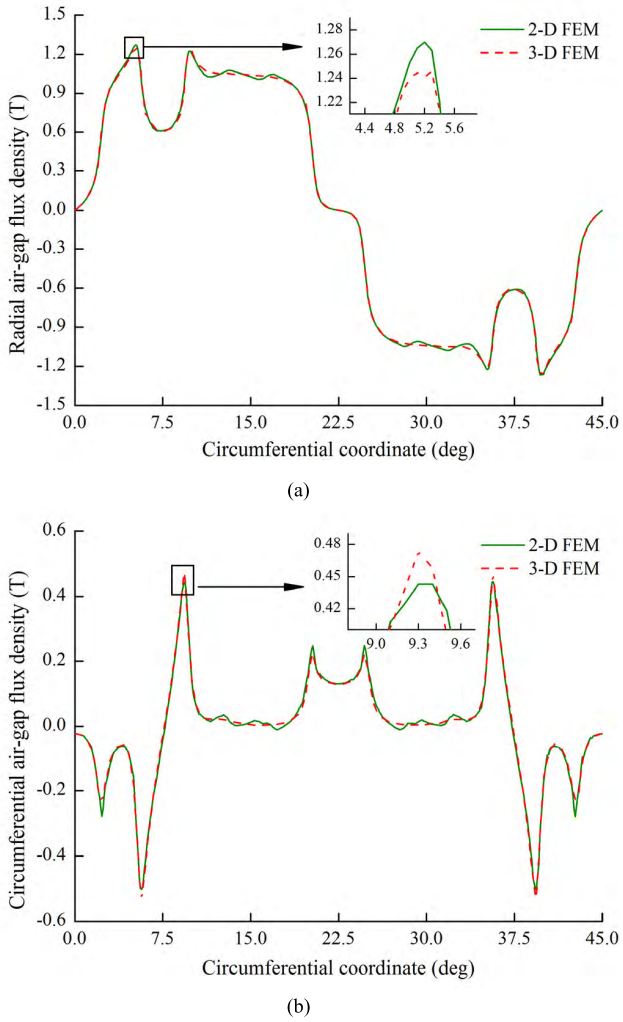

FIGURE 4. Air-gap flux densities in the axial middle of the machine. (a) Radial components. (b) Circumferential components.

not the case. Fig. 4 shows B_r and B_θ versus the circumferential coordinate (θ) in the plane $z = L/2$. It can be observed that there are some discrepancies between the analysis results obtained from the 2-D and 3-D FEMs, especially at the peak points. The discrepancies are mainly caused by the differences between the 2-D and 3-D FE solvers. For example, the 2-D FE solver adopts the magnetic vector potential to solve the magnetic field, but the magnetic scalar potential is applied in the 3-D FE solver [23], [24]. These differences will lead to numerical errors in the calculation of the field in the air-gap, especially for the points where the flux densities change drastically.

In the method in the literature [14]–[16], the axial distribution of the ratio of peak radial air-gap flux densities obtained from the 3-D and 2-D FEMs is used to quantify the end leakage flux. However, the analysis results deduced by this approach are susceptible to numerical errors because only the datum at the peak point on each plane $z = z_i$, $0 \le z_i \le L/2$, is used.

In this paper, to obtain more reliable conclusions and better analyze the impact of numerical errors, air-gap flux densities at all points on each plane $z = z_i$ are employed to analyze the end leakage flux. The proposed end leakage flux function consists of a radial air-gap flux density distribution function along the axial direction (RAFDDFAD) $f_{Br}(z)$ and a circumferential air-gap flux density distribution function along the axial direction (CAFDDFAD) $f_{B\theta}(z)$. They are expressed as follows:

$$f_{B_r}(z) = \frac{\int_0^{2\pi} |B_{r-3D}(\theta, z)| \cdot d\theta}{\int_0^{2\pi} |B_{r-2D}(\theta)| \cdot d\theta}, \tag{1}$$

$$f_{B_\theta}(z) = \frac{\int_0^{2\pi} |B_{\theta-3D}(\theta, z)| \cdot d\theta}{\int_0^{2\pi} |B_{\theta-2D}(\theta)| \cdot d\theta}, \tag{2}$$

where $|B_{r-3D}(\theta, z)|$ and $|B_{r-2D}(\theta)|$ are the magnitudes of the radial air-gap flux densities calculated by the 3-D and 2-D

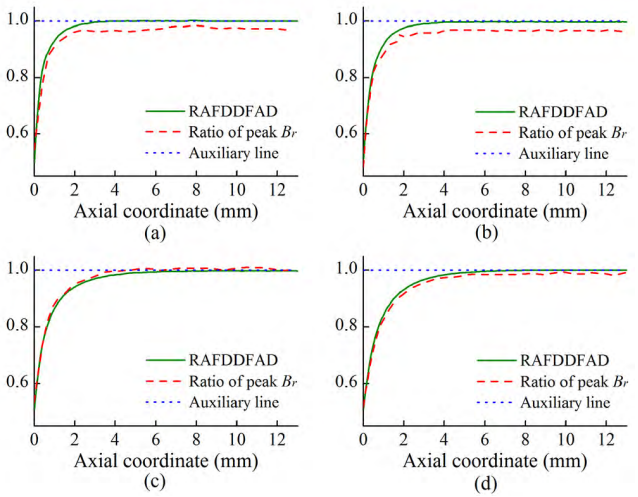

FIGURE 5. Curves used to analyze the influence of the end leakage flux on the radial air-gap magnetic field. (a), (b), (c), and (d) show four different sets of parameters.

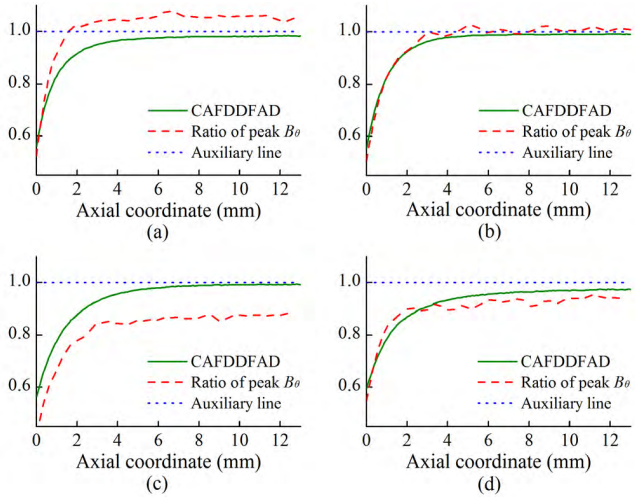

FIGURE 6. Curves employed to analyze the influence of the end leakage flux on the circumferential air-gap magnetic field. (a), (b), (c), and (d) show four different sets of parameters.

FEMs, respectively. Similarly, $|B_{\theta-3D}(\theta, z)|$ and $|B_{\theta-2D}(\theta)|$ are the magnitudes of the circumferential air-gap flux densities obtained from the 3-D and 2-D FEMs, respectively.

The RAFDDFADs and CAFDDFADs of the topology calculated by equations (1) and (2) are shown in Figs. 5 and 6, respectively. In addition, the auxiliary lines with an identity of 1, which indicate where the same results were obtained for the 2-D and 3-D calculations, are drawn in Figs. 5 and 6. It can be seen that all RAFDDFADs converge to 1 with the increase of z, which indicates that the differences between the 2-D and 3-D FE solvers barely impact the analysis of the influence of the end leakage flux on the radial air-gap magnetic field. However, there are a few discrepancies between CAFDDFADs and the auxiliary lines in the axial middle of the machine, which reveals that the differences between the FE solvers impact the analysis of the influence of the end leakage flux on the circumferential air-gap magnetic field. This result can be explained by the fact that, compared with B_r, B_θ is much smaller, and therefore, the relative numerical errors caused by the differences are larger.

For comparison, the axial distribution curves of the ratios of the peak air-gap flux densities obtained from the 3-D and 2-D FEMs are also shown in Fig. 5 and 6, which is equivalent to the method in [14]–[16]. As expected, if only the datum of the peak point on each plane $z = z_i$ is used to analyze the end leakage flux, the obtained results are heavily impacted by the numerical errors caused by the differences between the FE solvers.

From Figs. 5 and 6, it can be seen that the end leakage flux has a diverse influence on the radial and circumferential air-gap magnetic fields, which means that it is necessary to use two different functions to describe the axial distributions of the two air-gap magnetic fields.

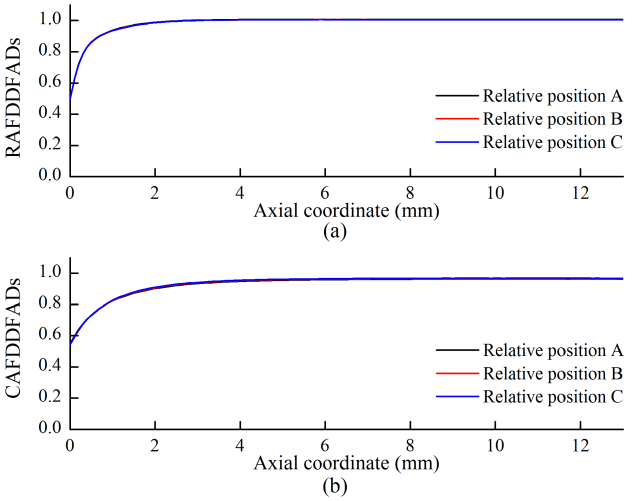

FIGURE 7. Depiction of the end leakage flux functions for different relative positions between the rotor and the stator. (a) RAFDDFADs. (b) CAFDDFADs.

Fig. 7 shows the obtained RAFDDFADs and CAFDDFADs of the topology with the first set of parameters when the rotor is located at different positions relative to the stator. At relative positions A, B, and C, i.e., 0 deg, 1.5 deg, and 6 deg, the cogging torque of the machine is equal to zero, positive peak, and negative peak, respectively. It can be observed that neither RAFDDFAD nor CAFDDFAD change with the relative position between the rotor and the stator.

III. SENSITIVITY ANALYSIS OF THE END LEAKAGE FLUX IN FSCWSPM MACHINES

A. PRIMARY SELECTION OF THE DIMENSIONAL PARAMETERS

Fig. 8 shows the motor topology equivalent to a linear translation, which is suitable for any specific FSCWSPM machine. The dominant leakage flux paths are paths 1 to 3 within the length of the armature and path 4 at the end.

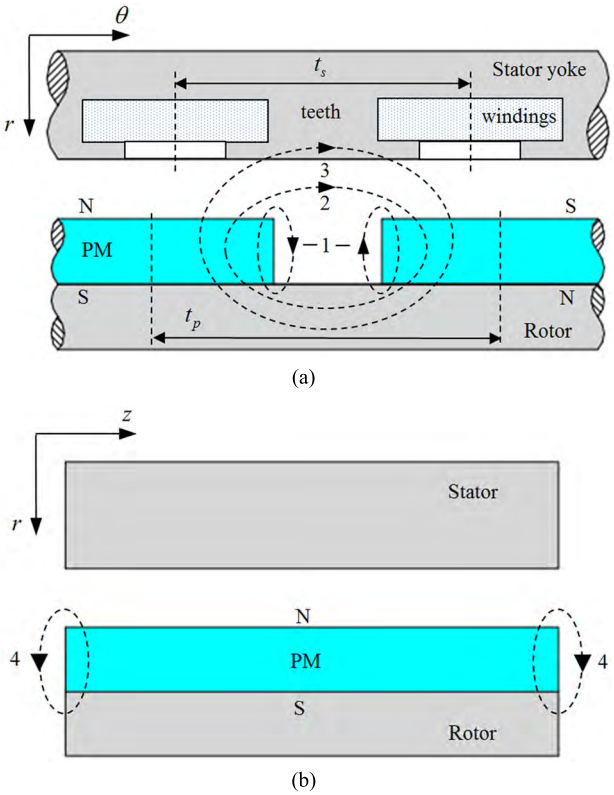

FIGURE 8. Leakage flux paths of an FSCWSPM machine. (a) Within the length of the armature. (b) At the end.

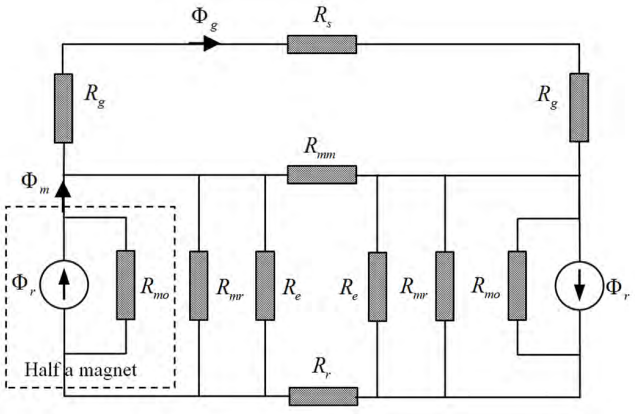

FIGURE 9. EMC of half of the magnet pole pair.

For the 3-D EMC method, to simplify the problem, the following assumptions are introduced: 1) infinite permeable iron materials are used, and 2) the magnetic field intensity produced by the armature current is negligible. Therefore, the EMC of half of the magnet pole pair shown in Fig. 9 can be reduced to Fig. 10, for which the variables are defined as follows:

- Φ_r flux source produced by half of the magnet pole pair;
- Φ_m total flux provided by half of the magnet pole pair to the external magnetic circuit;

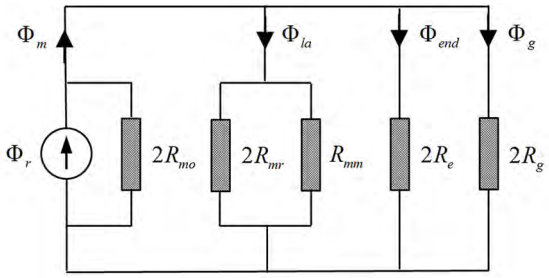

FIGURE 10. A reduced form of Fig. 9.

- Φ_g flux passing through the air-gap cross-sectional area facing half of the magnet pole;
- Φ_{la} leakage flux within the length of the armature;
- Φ_{end} end leakage flux of half of the magnet pole pair;
- R_{mo} half of the reluctance corresponding to Φ_r;
- R_g reluctance corresponding to Φ_g;
- R_{mr} reluctance corresponding to the magnet-to-rotor leakage flux of half of the magnet pole within the length of the armature;
- R_{mm} reluctance corresponding to the magnet-to-magnet leakage flux of half of the magnet pole pair within the length of the armature;
- R_e half of the reluctance corresponding to Φ_{end};
- R_s reluctance of the stator back iron;
- R_r reluctance of the rotor back iron.

By flux division, Φ_{end} and Φ_m can be obtained, respectively, as

$$\Phi_{end} = \frac{\lambda}{1+\eta+\lambda+\upsilon+2\xi} \cdot \Phi_r \tag{3}$$

and

$$\Phi_m = \frac{\eta+\lambda+\upsilon+2\xi}{1+\eta+\lambda+\upsilon+2\xi} \cdot \Phi_r \tag{4}$$

Hence, the end leakage flux coefficient k_{end} can be obtained as

$$k_{end} = \frac{\eta+\upsilon+2\xi}{\eta+\lambda+\upsilon+2\xi} \tag{5}$$

In equations (3)–(5), η is the ratio of R_{mo} to R_{mr}, λ is the ratio of R_{mo} to R_e, ξ is the ratio of R_{mo} to R_{mm} and υ is the ratio of R_{mo} to R_g. R_{mo} is calculated as

$$R_{mo} = \frac{2h_m}{\mu_0\mu_r w_m L} \tag{6}$$

R_{mr} is expressed as

$$R_{mr} = 1 \Big/ \left[\frac{\mu_0 L}{\pi} \ln\left(1+\frac{\pi g_e}{h_m}\right)\right] \tag{7}$$

R_e is written as

$$R_e = 1 \Big/ \left[\frac{4\mu_0 w_m}{3\pi} \ln\left(1+\frac{3\pi g_e}{2h_m}\right)\right] \tag{8}$$

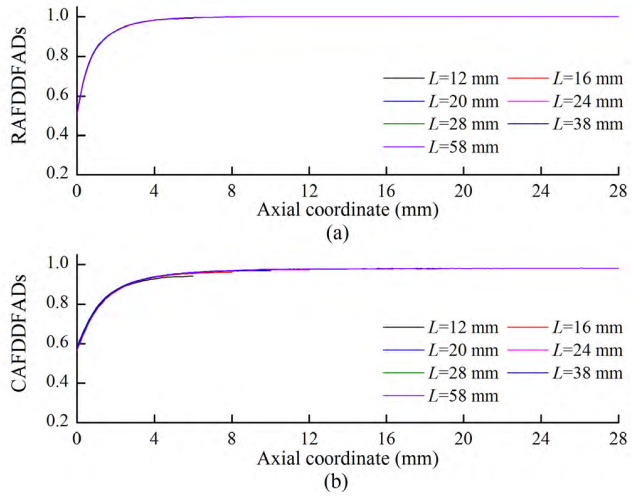

FIGURE 11. Influence of the axial length on the end leakage flux. (a) RAFDDFADs. (b) CAFDDFADs.

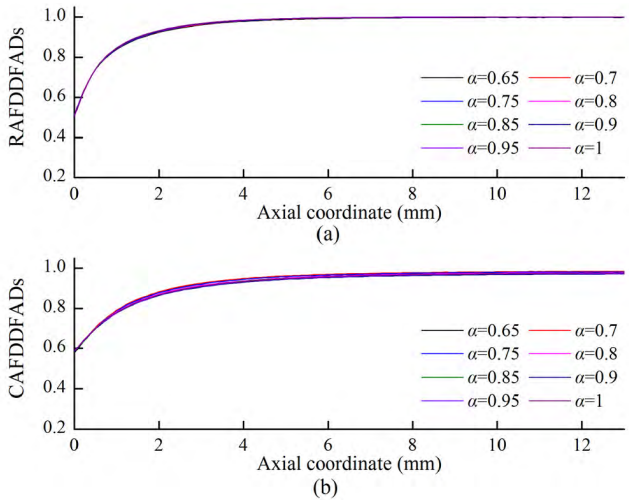

FIGURE 12. Influence of the pole-arc coefficient on the end leakage flux. (a) RAFDDFADs. (b) CAFDDFADs.

R_{mm} is

$$R_{mm} = 1 \Big/ \left[\frac{\mu_0 L}{\pi} \ln(1 + \frac{\pi g_e}{w_f}) \right] \tag{9}$$

and R_g is

$$R_g = \frac{2g_e}{\mu_0(w_m + 2g_e)L} \tag{10}$$

where μ_0 is the permeability of air, μ_r is the relative permeability of the PMs, h_m is the magnet thickness, and w_m is the width of one magnet pole, which is expressed as

$$w_m = \alpha t_p \tag{11}$$

w_i is the interval between magnet poles, which is calculated by

$$w_i = (1 - \alpha)\, t_p \tag{12}$$

α is the pole-arc coefficient, t_p is the pole pitch, and g_e is the effective length of the air-gap, taking the stator slotting into account, which can be obtained as

$$g_e = g \frac{t_s(5g + b_{s0})}{t_s(5g + b_{s0}) - b_{s0}^2} \tag{13}$$

t_s is the slot pitch, g is the actual length of the air-gap, and b_{s0} is the slot opening width.

For convenience of discussion, the slot opening width ratio is defined as

$$\gamma = \frac{b_{s0}}{t_s} \tag{14}$$

Based on equations (3)–(14), the dimensional parameters that might influence the end leakage flux of an FSCWSPM machine are L, α, h_m, g and γ.

B. INFLUENCE OF THE ABOVE PARAMETERS

As shown in Fig. 11, the calculated RAFDDFADs fall into nearly a locus when L changes and the other parameters remain constant. Thus, these distribution functions can be expressed by an equation and only the defined domain varies

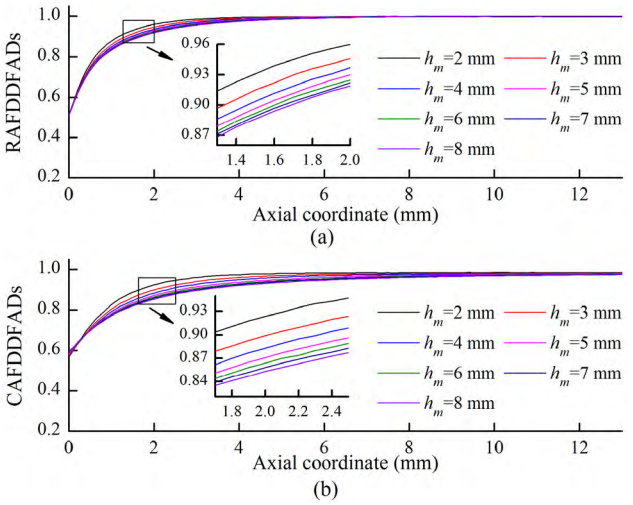

FIGURE 13. Influence of the magnet thickness on the end leakage flux. (a) RAFDDFADs. (b) CAFDDFADs.

with L. The CAFDDFADs have the same characteristics as the RAFDDFADs. As depicted in Fig. 12, the variation in α has no obvious influence on the axial distributions of the radial and circumferential air-gap flux densities. From Fig. 13, it can be clearly observed that both RAFDDFAD and CAFDDFAD change with h_m. The variation in g leads to a large change in RAFDDFAD and CAFDDFAD, as shown in Fig. 14. γ has a significant influence on the axial distribution of the circumferential air-gap flux density but no impact on the distribution of the radial air-gap flux density, as described in Fig. 15. In other words, the principal dimensional parameters that affect the end leakage flux in an FSCWSPM machine are h_m, g and γ.

From Figs. 11-15, it can also be seen that, regardless of the values of α, h_m, g, and γ, the RAFDDFADs always converge to 1 as L increases. However, under the impact of the differences between the 2-D and 3-D FE solvers, the convergence

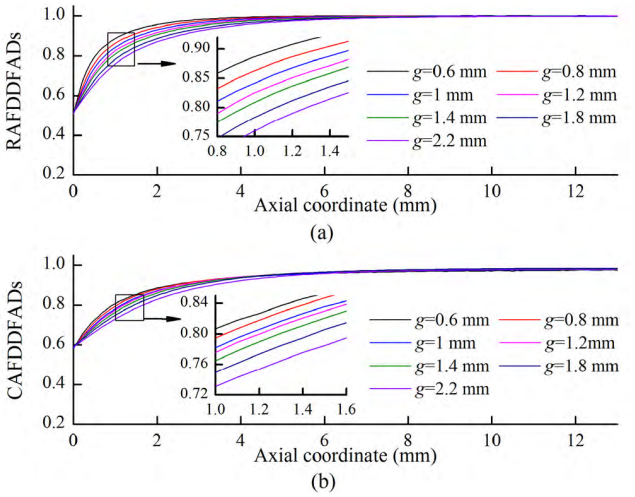

FIGURE 14. Influence of the air-gap length on the end leakage flux. (a) RAFDDFADs. (b) CAFDDFADs.

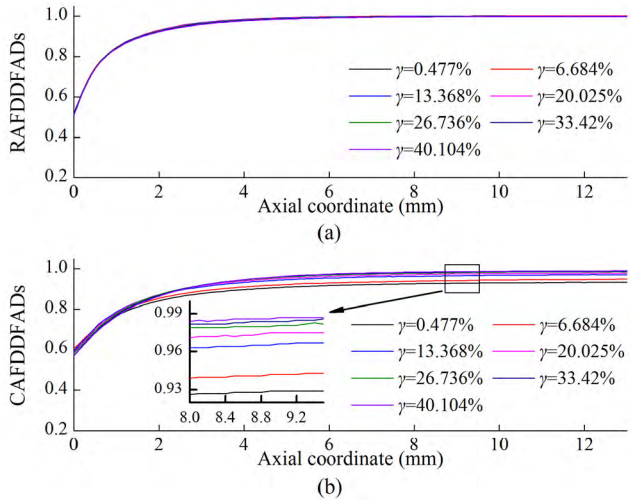

FIGURE 15. Influence of the slot opening width ratio on the end leakage flux. (a) RAFDDFADs. (b) CAFDDFADs.

value of the CAFDDFADs depends on h_m, g, and γ. In this paper, the numerical errors caused by the differences are accounted for in the parametric model established in the next section for obtaining analysis results that are similar to the results calculated by the 3-D FEM.

IV. PARAMETRIC MODELING OF THE PROPOSED END LEAKAGE FLUX FUNCTION IN FSCWSPM MACHINES

The proposed end leakage flux function can precisely describe the influence of the end leakage flux on the axial distribution of the air-gap magnetic field in an FSCWSPM machine. However, acquiring the end leakage flux function for a given machine by equations (1) and (2) still requires significant FE programming and computational time. It may not be acceptable during the initial design and optimization stages because a tremendous number of samples need to be calculated with continually modified dimension parameters.

TABLE 2. Level combinations between the magnet thickness and the air-gap length.

h_m (mm) \ g (mm)	0.4	0.6	0.8	1	1.2	1.4
2	✓	✓	✓			
2.75	✓	✓	✓	✓		
3.5	✓	✓	✓	✓	✓	
4.25	✓	✓	✓	✓	✓	✓
5	✓	✓	✓	✓	✓	✓
5.75		✓	✓	✓	✓	✓
6.5			✓	✓	✓	✓
7.25				✓	✓	✓
8					✓	✓
8.75						✓

Therefore, it is necessary to establish a simple parametric model to rapidly construct the end leakage flux function.

For an FSCWSPM machine, when the material properties are given, the proposed end leakage flux function depends mainly on the dimensional parameters h_m, g, and γ, which can be known according to the studies mentioned in the Section III. Useful ranges for these dimensional parameters, i.e., ranges that are suitable for the FSCWSPM machines usually encountered in practice, can be defined. For such machines, h_m ranges from 2 to 8.75 mm, g ranges from 0.4 to 1.4 mm, and γ ranges from 6.684 to 46.8%. In general, in the design of PM machines, h_m is related to g. To ensure the appropriate magnetic load, the longer g is, the thicker h_m will be. Therefore, the design of the experiment obeys the following rules: 1) g has 6 levels and γ has 7 levels; 2) the level combinations between h_m and g are shown in Table 2, in which the symbol $\surd$ indicates that the corresponding combination is valid; and 3) the full factor experiment is arranged between γ and the combinations shown in Table 2. Thus, there are 273 samples that need to be analyzed.

The proposed equations (1) and (2) are, respectively, used to calculate the RAFDDFADs and CAFDDFADs for the 273 samples. Based on experience and the calculation results of these samples, the RAFDDFADs can be fitted by

$$f_{B_r}^{P}(z)=\begin{cases} s_r(z)=-\dfrac{1}{A_r\cdot(z+B_r)}+C_r, & z|s_r(z)\le 1 \\ 1, & z|s_r(z)>1, \end{cases} \tag{15}$$

and the CAFDDFADs can be fitted by

$$f_{B_\theta}^{P}(z)=\begin{cases} s_\theta(z)=-\dfrac{1}{A_\theta\cdot(z+B_\theta)}+C_\theta, & z|s_\theta(z)\le D \\ D, & z|s_\theta(z)>D. \end{cases} \tag{16}$$

In equations (15) and (16), $s_r(z)$ and $s_\theta(z)$ are temporary functions. A_r, B_r, C_r, A_θ, B_θ, C_θ and D can be approximately written as

$$y_i=\prod_{j=1}^{3}\left(\beta_{ij0}+\beta_{ij1}\cdot x_j^1+\beta_{ij2}\cdot x_j^2\right),\quad i=1,2,3,4,5,6,7. \tag{17}$$

In equation (17), y_i, $i=1$ to 7, are A_r, B_r, C_r, A_θ, B_θ, C_θ, and D, respectively. x_j, $j=1$, 2, and 3, are h_m, g,

and γ, respectively. β_{ij0}, β_{ij1}, and β_{ij2} are the target coefficients to be searched. The target coefficients can be acquired by means of the nonlinear regression of the calculation results obtained from the above 273 samples. For FSCWSPM machines, the target coefficients of the RAFDDFADs and CAFDDFADs are listed in Tables 3 and 4, respectively.

TABLE 3. Target coefficients of the RAFDDFADs

A_r		B_r		C_r	
Item	Value	Item	Value	Item	Value
β_{110}	0.922	β_{210}	0.0101	β_{310}	0.2672
β_{111}	-1.0379	β_{211}	0.1123	β_{311}	0.0137
β_{112}	0.3826	β_{212}	-0.0148	β_{312}	-0.0037
β_{120}	27.7133	β_{220}	16.5758	β_{320}	17.6214
β_{121}	-1.968	β_{221}	2.0927	β_{321}	-0.1285
β_{122}	0.1328	β_{222}	-0.1209	β_{322}	0.0072
β_{130}	0.511	β_{230}	0.2284	β_{330}	0.2215
β_{131}	-0.0656	β_{231}	0.0089	β_{331}	0.0007
β_{132}	0.2822	β_{232}	-0.0257	β_{332}	-0.0099

TABLE 4. Target Coefficients of the CAFDDFADs.

A_θ		B_θ		C_θ		D	
Item	Value	Item	Value	Item	Value	Item	Value
β_{410}	0.6169	β_{510}	0.0783	β_{610}	0.2608	β_{710}	0.2638
β_{411}	-0.5496	β_{511}	0.1236	β_{611}	0.025	β_{711}	0.0051
β_{412}	0.1966	β_{512}	-0.0292	β_{612}	-0.0086	β_{712}	-0.0019
β_{420}	22.9047	β_{520}	13.3756	β_{620}	17.5453	β_{720}	17.264
β_{421}	-2.6684	β_{521}	3.4538	β_{621}	-0.1617	β_{721}	-0.0157
β_{422}	0.1864	β_{522}	-0.1823	β_{622}	0.0081	β_{722}	-0.0002
β_{430}	0.7282	β_{530}	0.2455	β_{630}	0.208	β_{730}	0.206
β_{431}	-1.2945	β_{531}	-0.1236	β_{631}	0.0774	β_{731}	0.055
β_{432}	1.0335	β_{532}	0.4642	β_{632}	-0.0784	β_{732}	-0.069

V. APPLICATION

The proposed end leakage flux function and its parametric model can be applied to correct the analysis results obtained from the 2-D FEM or AM. In these 2-D methods, all the field quantities are considered to be invariant in the axial direction. The revised radial and circumferential air-gap flux densities are expressed as follows:

$$\begin{aligned} B_{r-re}(r,\theta,z) &= f_{B_r}(z)\cdot B_{r-2D}(r,\theta) \\ &\approx f^P_{B_r}(z)\cdot B_{r-2D}(r,\theta) \end{aligned} \tag{18}$$

$$\begin{aligned} B_{\theta-re}(r,\theta,z) &= f_{B_\theta}(z)\cdot B_{\theta-2D}(r,\theta) \\ &\approx f^P_{B_\theta}(z)\cdot B_{\theta-2D}(r,\theta) \end{aligned} \tag{19}$$

In equations (18) and (19), $B_{r-re}(r,\theta,z)$ and $B_{\theta-re}(r,\theta,z)$ are used to approximate the 3-D FEM calculated radial and circumferential air-gap flux densities, respectively. $B_{r-2D}(r,\theta)$ and $B_{\theta-2D}(r,\theta)$ are, respectively, the radial and circumferential air-gap flux densities obtained from the 2-D FEM.

The magnetic stress vector on the enclosed surface is given by [25]

$$\vec{f}_m = \frac{1}{\mu_0}\left(B_r^2 - \frac{1}{2}\left|\vec{B}\right|^2\right)\vec{e}_r + \frac{1}{\mu_0}B_r B_\theta \vec{e}_\theta \tag{20}$$

There are two components in the magnetic stress vector. One component is the radial component f_r, which can be used to approximate the radial force in actual PM machines, and the other component is the circumferential component f_θ, which can be used to approximate the circumferential force.

When the end leakage flux cannot be ignored, the cogging torque of FSCWSPM machines can be approximately written in integral form as

$$\begin{aligned} &Tc_{re} \\ &= \frac{1}{\mu_0}\iint_S R\cdot B_{r-re}(r,\theta,z)\cdot B_{\theta-re}(r,\theta,z)\,dS \\ &= \frac{1}{\mu_0}\iint_S R\cdot B_{r-2D}(r,\theta)\cdot f_{B_r}(z)\cdot B_{\theta-2D}(r,\theta)\cdot f_{B_\theta}(z)\,dS \\ &= \frac{1}{L}\int_0^L f_{B_r}(z)\cdot f_{B_\theta}(z)\,dz\cdot L\frac{1}{\mu_0}\int_0^{2\pi} R^2 \\ &\quad\cdot B_{r-2D}(r,\theta)\cdot B_{\theta-2D}(r,\theta)\,d\theta \\ &= k_{Tc}\cdot Tc_{2D} \\ &\approx \frac{1}{L}\int_0^L f^P_{B_r}(z)\cdot f^P_{B_\theta}(z)\,dz\cdot L\frac{1}{\mu_0}\int_0^{2\pi} R^2 \\ &\quad\cdot B_{r-2D}(r,\theta)\cdot B_{\theta-2D}(r,\theta)\,d\theta \\ &\approx k^P_{Tc}\cdot Tc_{2D} \end{aligned} \tag{21}$$

where R is the radius of the integration surface; S is the integration surface; Tc_{re} is the revised cogging torque, which is used to approximate the cogging torque calculated by the 3-D FEM; Tc_{2D} is the cogging torque calculated by the 2-D FEM; k_{Tc} is the torque coefficient based on equations (1) and (2); and k^P_{Tc} is the torque coefficient deduced by equations (15) and (16). k_{Tc} and k^P_{Tc} are expressed as follows:

$$k_{Tc} = \frac{1}{L}\int_0^L f_{B_r}(z)\cdot f_{B_\theta}(z)\,dz, \tag{22}$$

$$k^P_{Tc} = \frac{1}{L}\int_0^L f^P_{B_r}(z)\cdot f^P_{B_\theta}(z)\,dz. \tag{23}$$

TABLE 5. Parameters of Machines 1–4.

Parameter (unit)	Machine 1	Machine 2	Machine 3	Machine 4
Slot/pole combination	12/8	12/10	48/32	18/24
Magnet thickness (mm)	4.875	2	6.3	4.5
Embrace	0.8	0.79	0.75	0.82
Air-gap length (mm)	1.235	0.6	1.2	0.9
Slot opening width ratio	18.11%	16.18%	26.84%	19.83%
Air-gap diameter (mm)	80.12	47.2	284.6	130
Axial length (mm)	24.65	20	40	19
Rotor position	inner	inner	outer	inner
Supply voltage (V)	48	24	336	220
Outer diameter (mm)	142	70.5	312	180
Peak output power (kW)	0.6	0.07	20	3.75

VI. VALIDATION

Table 5 lists the design parameters of four FSCWSPM machines that are analyzed to evaluate the precision and adaptability of the proposed end leakage flux function and

its parametric model. These machines have different slot/pole combinations, magnet thicknesses, embraces, air-gap lengths, slot opening width ratios, air-gap diameters, axial lengths, outer diameters, peak output powers, etc. Moreover, these machines are equipped with three-phase windings.

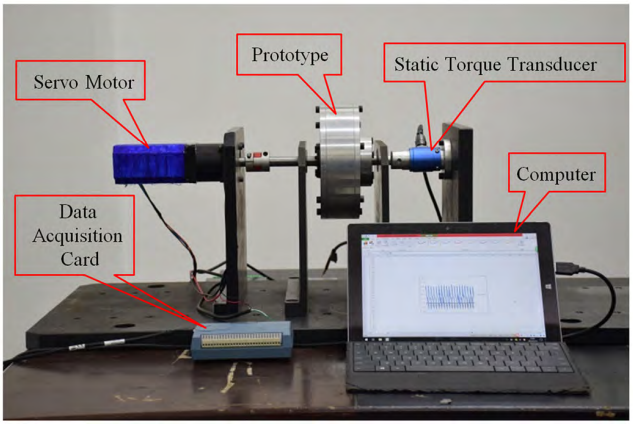

FIGURE 16. Test platform of the prototype.

Machine 1 is manufactured and tested. A photograph of the experimental platform is shown in Fig. 16. The cogging torque of the prototype is measured by a static torque transducer with a full scale of 1 Nm and a precision of 0.1%. The rotor of the prototype is driven by a servo motor at a speed of 2 rpm. The stator is connected to the static torque transducer that is mounted on the base frame. Because of manufacturing errors, there are a few discrepancies between the actual dimensions and the design of the prototype. To eliminate the influence of manufacturing errors, the dimensions in the 2-D and 3-D FE models are adjusted to the actual values for the prototype. For example, the air-gap length is adjusted from 1.2 mm to 1.235 mm, and the axial length is adjusted from 24.5 mm to 24.65 mm.

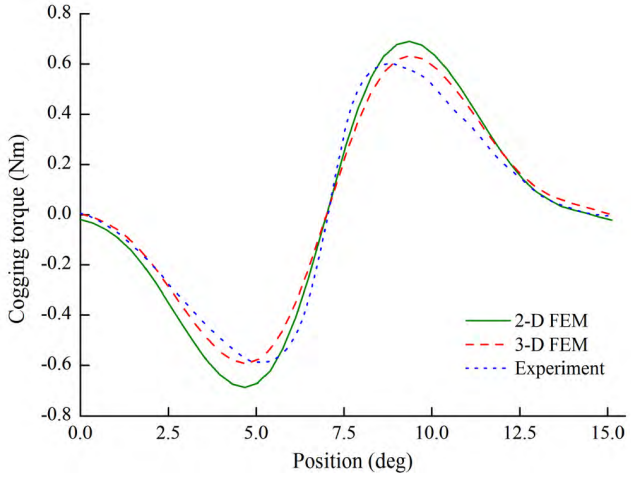

FIGURE 17. Comparison of the cogging torques obtained from the experiment and the 2-D and 3-D FEMs.

Fig. 17 compares the cogging torques of Machine 1 obtained from the experiment and the 2-D and 3-D FE simulations. It is worth noting that the DC bias component caused by the eddy current loss and hysteresis loss is difficult to observe in the test waveform. According to the modified Steinmetz equation, the eddy current loss is proportional to the square of the frequency, and the hysteresis loss is proportional to the frequency. Therefore, the lower the motor speed, the lower the eddy current loss and the hysteresis loss, the lower the signal-to-noise ratio of the DC bias component, and the harder the component is to measure. From Fig. 17, it can be seen that the amplitude of the cogging torque calculated by the 3-D FEM agrees well with that obtained from the experiment. However, the waveform obtained from the experiment deviates from that simulated by the 3-D and 2-D FEMs due to the small torsional stiffness of the measurement system.

It is well known that the cogging torque depends on the relative position between the rotor and the stator. When the cogging torque is loaded by the stator in the small-torque measurement system, a small torsion occurs due to the small torsional stiffness. Because of the small torsion, the relative position between the rotor and the stator differs from the rotation angle of the rotor. The relative position and the rotation angle are equal only when the cogging torque is zero. In other words, the small torsional stiffness of the measurement system will hinder an increase in the cogging torque along the rotor rotation direction and accelerate a decrease in the cogging torque along the rotor rotation direction. Nevertheless, it will not change the amplitude of the cogging torque, as shown in Fig. 17.

According to the comparison in Fig. 17, the FE programming and solutions in this paper can be assured to be accurate enough to get reliable conclusions. Additionally, because the end leakage flux is not accounted for in the 2-D FEM, the cogging torque obtained from the 2-D FEM is obviously larger than those obtained from the experiment and the 3-D FEM.

Fig. 18 compares the RAFDDFADs calculated by the parametric model (15) with those obtained from the FEM, i.e., equation (1), for Machines 1-4. A comparison between the CAFDDFADs calculated by the parametric model (16) and those obtained from equation (2) is presented in Fig. 19. Whether they are RAFDDFADs or CAFDDFADs, the results from the parametric model and equations (1)-(2) agree well.

In Fig. 20, the cogging torques revised by the proposed end leakage flux function and parametric model, namely, that calculated by equation (21), are compared with the corresponding simulation results from the 2-D and 3-D FEMs for Machines 1-4. Excellent agreement is observed between the 3-D FE simulated and revised cogging torques. As expected, the results simulated by the 2-D FEM are significantly larger than those obtained from the 3-D FEM and the revised results because the end leakage flux is not accounted for.

The obtained torque coefficients k_{Tc} and k_{Tc}^{P} are listed in Table 6. It can be observed that the end leakage flux has obvious an influence on the performance analysis of Machines 1-4 due to their short axial lengths. The minimum

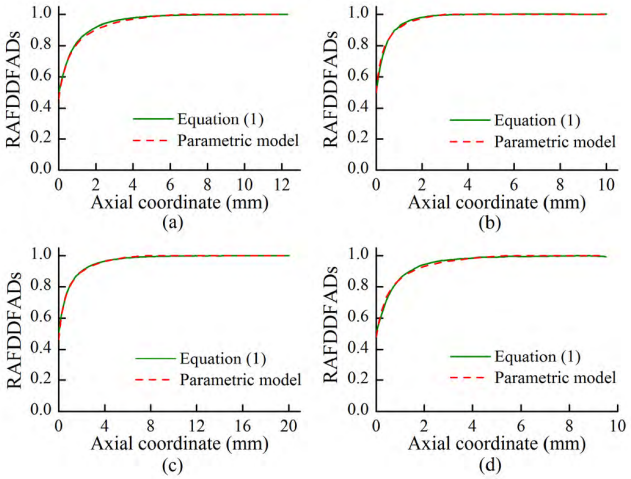

FIGURE 18. Comparisons between the RAFDDFADs calculated by the parametric model and those from equation (1). (a) Machine 1. (b) Machine 2. (c) Machine 3. (d) Machine 4.

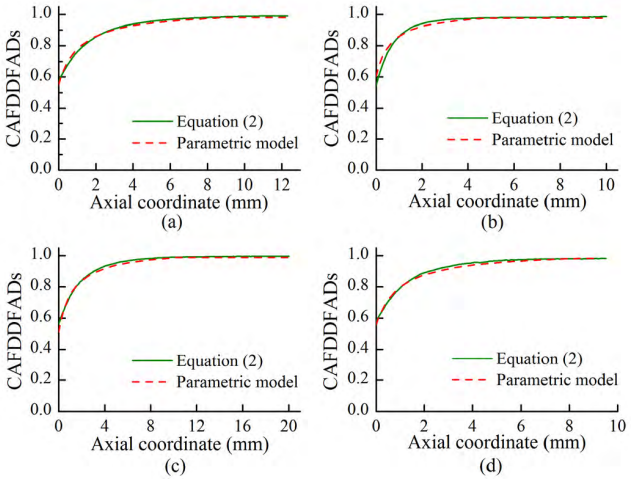

FIGURE 19. Comparisons between the CAFDDFADs calculated by the parametric model and those from equation (2). (a) Machine 1. (b) Machine 2. (c) Machine 3. (d) Machine 4.

TABLE 6. Torque coefficients of Machines 1–4 obtained from the FEM and the parametric model.

Item	k_{Tc}	k_{Tc}^{P}
Machine 1	0.894	0.886
Machine 2	0.925	0.92
Machine 3	0.925	0.919
Machine 4	0.884	0.877

and maximum axial lengths of these machines are 19 and 40 mm, respectively. For a machine with a shorter axial length, the influence of the end leakage flux will be more significant.

The calculation results were obtained on an Intel(R) Core(TM) i5-7400 CPU @ 3-GHz with a 16-GB memory. Table 7 lists the time taken to get the revised cogging torques and the cogging torques calculated via 3-D FEM. Only a few

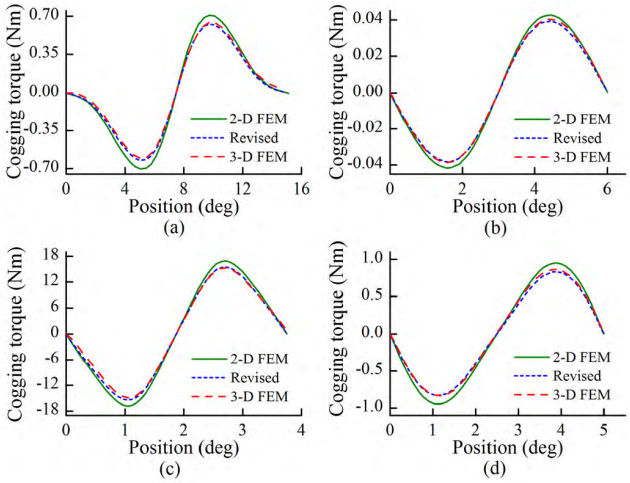

FIGURE 20. Comparison of the revised, 2-D, and 3-D FE simulated cogging torques. (a) Machine 1. (b) Machine 2. (c) Machine 3. (d) Machine 4.

TABLE 7. Time needed to get the revised cogging torques and the cogging torques calculated via 3-D FEM.

Item	Proposed methodology	3-D FEM
Machine 1	0 h, 2 min and 12 s	12 h, 51 min and 36 s
Machine 2	0 h, 1 min and 47 s	8 h, 5 min and 0 s
Machine 3	0 h, 4 min and 0 s	27 h, 51 min and 36 s
Machine 4	0 h, 1 min and 48 s	7 h, 17 min and 24 s

minutes are needed to obtain the revised cogging torques using the proposed end leakage flux function and its parametric model. However, many hours are needed to obtain the cogging torques by using the 3-D FEM.

Comparisons in Figs. 18-20 and Tables 6-7 reveal that the proposed end leakage flux function and its parametric model have good precision and adaptability for FSCWSPM machines of different sizes and output powers and indicate that a significant amount of time can be saved by using this method, which is very meaningful for the initial design and optimization of FSCWSPM machines with nonnegligible end leakage flux.

VII. CONCLUSIONS

In this paper, a novel end leakage flux function, which consists of RAFDDFAD and CAFDDFAD, is proposed. The end leakage flux function can be used to precisely quantify the end leakage flux of FSCWSPM machines for the following reasons: 1) the air-gap flux densities at all points on each plane $z = z_i$ are used to deduce RAFDDFAD and CAFDDFAD to alleviate the impact of numerical errors caused by the differences between the 2-D and 3-D FE solvers; 2) two functions, i.e., RAFDDFAD and CAFDDFAD, are adopted to describe the influence of the end leakage flux on the axial distributions of the radial and circumferential air-gap magnetic fields, respectively; and 3) the relative positions of the stator and the rotor do not impact the precision of the proposed end leakage flux function.

The sensitivity analysis indicates that the PM thickness, air-gap length and slot opening width ratio have a significant influence on the distribution of the end magnetic field of the FSCWSPM machines, but the distribution does not change with the axial length. In addition, for a PM machine with a shorter axial length, the ratio of the end leakage flux to the total air-gap flux will be larger, and so the influence of the end leakage flux will be more obvious.

Based on 273 samples, a parametric model consisting of (15) and (16) is established. Equations (15) and (16) can be used to quickly construct RAFDDFAD and CAFDDFAD, respectively. In addition, the numerical errors caused by the differences between the FE solvers are also accounted for in the parametric model because the purpose of this paper is to obtain results that are very close to those of the 3-D FE analysis.

By taking the cogging torque calculation as an example, the application of the above end leakage flux function and parametric model is briefly described.

With the help of the proposed end leakage flux function and its parametric model, the analysis of FSCWSPM machines with nonnegligible end leakage flux is reduced to a 2-D issue. As a result, the solution time and resources can be significantly reduced during the initial design and optimization because the performance of the machine needs to be calculated many times with continually modified dimension parameters.

Finally, the FE analysis and experimental results verify the calculation precision, adaptability, and timeliness of the proposed methodology for FSCWSPM machines of different sizes and output powers.

REFERENCES

[1] A. Dwivedi, S. K. Singh, and R. K. Srivastava, "Analysis of permanent magnet brushless AC motor using Fourier transform approach," *IET Elect. Power Appl.*, vol. 10, no. 6, pp. 539–547, Jul. 2016.

[2] D. Li, T. Zou, R. Qu, and D. Jiang, "Analysis of fractional-slot concentrated winding PM Vernier machines with regular open-slot stators," *IEEE Trans. Ind. Appl.*, vol. 54, no. 2, pp. 1320–1330, Mar./Apr. 2018.

[3] Z. Q. Zhu and Y. Liu, "Analysis of air-gap field modulation and magnetic gearing effect in fractional-slot concentrated-winding permanent-magnet synchronous machines," *IEEE Trans. Ind. Electron.*, vol. 65, no. 5, pp. 3688–3698, May 2018.

[4] S. G. Min and B. Sarlioglu, "Analysis and comparative study of flux weakening capability in fractional-slot concentrated windings," *IEEE Trans. Energy Convers.*, vol. 33, no. 3, pp. 1025–1035, Sep. 2018.

[5] M. Qiao, C. Jiang, y. Zhu, and G. Li, "Research on design method and electromagnetic vibration of six-phase fractional-slot concentrated-winding PM motor suitable for ship propulsion," *IEEE Access*, vol. 4, pp. 8535–8543, 2016.

[6] H. Li and T. Li, "End-effect magnetic field analysis of the halbach array permanent magnet spherical motor," *IEEE Trans. Magn.*, vol. 54, no. 4, Apr. 2018, Art. no. 8202209.

[7] R. Lin and A. Arkkio, "Calculation and analysis of stator end-winding leakage inductance of an induction machine," *IEEE Trans. Magn.*, vol. 45, no. 4, pp. 2009–2014, Apr. 2009.

[8] J.-W. Jung, H.-I. Park, J.-P. Hong, and B.-H. Lee, "A novel approach for 2-D electromagnetic field analysis of surface mounted permanent magnet synchronous motor taking into account axial end leakage flux," *IEEE Trans. Magn.*, vol. 53, no. 11, Nov. 2017, Art. no. 8208104.

[9] J. H. J. Potgieter and M. J. Kamper, "Calculation methods and effects of end-winding inductance and permanent-magnet end flux on performance prediction of nonoverlap winding permanent-magnet machines," *IEEE Trans. Ind. Appl.*, vol. 50, no. 4, pp. 2458–2466, Jul./Aug. 2014.

[10] Z. Q. Zhu, Y. Pang, W. Hua, M. Cheng, and D. Howe, "Investigation of end effect in permanent magnet brushless machines having magnets on the stator," *J. Appl. Phys.*, vol. 99, no. 8, Apr. 2006, Art. no. 08R319.

[11] Y.-J. Ge, C.-Y. Nie, and Q. Xin, "A three dimensional analytical calculation of the air-gap magnetic field and torque of coaxial magnetic gears," *Prog. Electromagn. Res.*, vol. 131, no. 2, pp. 391–407, Jan. 2012.

[12] R. Y. Tang, "Basic theory of permanent magnet synchronous motor and asynchronous starting permanent magnet synchronous motor," in *Modern Permanent Magnet Machines, Theory and Design*. Beijing, China: China Machine Press, 2016, pp. 220–225.

[13] Z. Z. Wu and Z. Q. Zhu, "Comparative analysis of end effect in partitioned stator flux reversal machines having surface-mounted and consequent pole permanent magnets," *IEEE Trans. Magn.*, vol. 52, no. 7, Jul. 2016, Art. no. 8103904.

[14] T. Shi, P. Song, H. Li, and C. Xia, "End-effect of the permanent-magnet spherical motor and its influence on back-EMF characteristics," *Sci. China Technol. Sci.*, vol. 55, no. 1, pp. 206–212, Jan. 2012.

[15] X. Zhu, M. Cheng, W. Hua, and J. Zhang, "Investigation of end-effect and experimental validation for hybrid excited doubly salient machine," in *Proc. 12th Biennial IEEE Conf. Electromagn. Field Comput.*, Miami, FL, USA, Apr./May 2006, p. 320.

[16] W. Hua and M. Cheng, "Static characteristics of doubly-salient brushless machines having magnets in the stator considering end-effect," *Elect. Power Compon. Syst.*, vol. 36, no. 7, pp. 754–770, Jul. 2008.

[17] R. Y. Tang, "Permanent magnet DC motor," in *Modern Permanent Magnet Machines: Theory and Design*. Beijing, China: China Machine Press, 2016, pp. 106–109.

[18] M. Sun, R. Tang, X. Han, and W. Tong, "Analysis and modeling for open circuit air gap magnetic field prediction in axial flux permanent magnet machines," *Proc. Chin. Soc. Elect. Eng.*, vol. 38, no. 5, pp. 1525–1533, Mar. 2018.

[19] W. Tong, S. Wang, S. Wu, and R. Tang, "A complete Quasi-3-D analytical model of no-load magnetic field of double-sided slotted AFPMMs considering end effect," *IEEE Access*, vol. 6, pp. 59557–59566, 2018.

[20] J. Azzouzi, G. Barakat, and B. Dakyo, "Quasi-3-D analytical modeling of the magnetic field of an axial flux permanent-magnet synchronous machine," *IEEE Trans. Energy Convers.*, vol. 20, no. 4, pp. 746–752, Dec. 2005.

[21] H. Tiegna, Y. Amara, and G. Barakat, "A new Quasi-3-D analytical model of axial flux permanent magnet machines," *IEEE Trans. Magn.*, vol. 50, no. 2, Feb. 2014, Art. no. 7020204.

[22] A. Di Gerlando, G. M. Foglia, M. F. Iacchetti, and R. Perini, "Evaluation of manufacturing dissymmetry effects in axial flux permanent-magnet machines: Analysis method based on field functions," *IEEE Trans. Magn.*, vol. 48, no. 6, pp. 1995–2008, Jun. 2012.

[23] W. N. Fu, P. Zhou, D. Lin, S. Stanton, and Z. J. Cendes, "Modeling of solid conductors in two-dimensional transient finite-element analysis and its application to electric machines," *IEEE Trans. Magn.*, vol. 40, no. 2, pp. 426–434, Mar. 2004.

[24] P. Zhou, Z. Badics, D. Lin, and Z. J. Cendes, "Nonlinear T- Ω formulation including motion for multiply connected 3-D problems," *IEEE Trans. Magn.*, vol. 44, no. 6, pp. 718–721, Jun. 2008.

[25] H. Hu, J. Zhao, X. Liu, Y. Guo, and J. Zhu, "No-load magnetic field and cogging force calculation in linear permanent-magnet synchronous machines with semiclosed slots," *IEEE Trans. Ind. Electron.*, vol. 64, no. 7, pp. 5564–5575, Jul. 2017.

XIANBAO CHEN received the graduation degree in vehicle engineering from the School of Automotive Engineering, Chongqing University, Chongqing, China, in 2016. He is currently pursuing the Ph.D. degree with the School of Automotive Engineering, Chongqing University, Chongqing, China. His research interests include electric machines and electric drive systems used for electric vehicles, especially in-wheel motor drive systems.

HONGYU SHU received the Ph.D. degree in mechanical engineering from Chongqing University, Chongqing, China, in 1999. He is currently a Professor with the State Key Laboratory of Mechanical Transmission, Chongqing University. His research interests include electric vehicles, mechatronics, vehicle noise, vibration and harshness, and vehicle system dynamics and control. He is currently a Senior Member of the Chinese Society of Mechanical Engineering.

YITONG SONG received the graduation degree in vehicle engineering from the College of Mechanical and Vehicle Engineering, Hunan University, Hunan, China, in 2016. He is currently pursuing the Ph.D. degree with the School of Automotive Engineering, Chongqing University, Chongqing, China. His research interests include integrated chassis control techniques for electric vehicles. He is currently working on integrated chassis control based on four-wheel steering and an active differential braking system of electric vehicles.

SHUANG LUO received the B.S. degree from the School of Automotive Engineering, Chongqing University, Chongqing, China, in 2013. He is currently pursuing the Ph.D. degree with the State Key Laboratory of Mechanical Transmission, Chongqing University. His research interests include the dynamics of human–machine systems, the vibrations of human-seat systems, and vehicle system dynamics.

CHENG GUO received the B.S. degree from the School of Automotive Engineering, Chongqing University, Chongqing, China, in 2017, where he is currently pursuing the M.S. degree. His main research interests include electric machine control and electric wheel drive systems.